stellarator news

Published by Fusion Energy Division, Oak Ridge National Laboratory
Building 9201-2 P.O. Box 2009 Oak Ridge, TN 37831-8071, USA

Editor: James A. Rome Issue 52 July 1997
E-Mail: jar@ornl.gov Phone (423) 574-1306 Fax: (423) 241-6211
On the Web at *http://www.ornl.gov/fed/stelnews*

*J** transport optimization of low-aspect-ratio stellarators

I. Introduction

Low-aspect-ratio, modular, tilted-coil stellarators [1–5] offer the attractive features of compact steady-state fusion power systems, high volume utilization, axisymmetric diverted regions, and the absence of low-order resonances (leading to islands) near the plasma edge. However, recent studies of confinement [3] in these devices have indicated the need for further transport optimization.

Of the two quasisymmetric approaches, only quasitoroidal optimizations have successfully been achieved [6] at low aspect ratio. The quasihelical approach [7] is expected to be applicable only at higher aspect ratios [8]. However, in parallel with the quasisymmetric approaches, various techniques for directly reducing the particle drifts away from magnetic flux surfaces have also been developed. Initial work [9] focused on improving the confinement of deeply trapped particles, since these orbits could be simply related to contours of the minimum of $|\boldsymbol{B}|$ along the toroidal direction.

We have developed a more general approach that improves the alignment of the approximate second adiabatic invariant [10,11] J^* contours with magnetic flux surfaces. This approach allows confinement improvement over the entire trapped particle population as well as a possible reduction in the number of transitional particles. Such an approach is equivalent to bounce-averaged omnigeneity, which has recently been interpreted [12–14] in terms of equal spacing of $|\boldsymbol{B}|$ contours on a magnetic flux surface. These methods are expected to open up a wider design space than the previous quasisymmetry approaches, since they place a weaker constraint on the form of the $|\boldsymbol{B}|$ spectrum. Besides improving confinement at low aspect ratio, this additional flexibility could allow for simultaneous optimization with respect to stability, bootstrap currents, and other physics criteria. We present an example of using the concept of bounce-averaged omnigeneity to generate an actual low-aspect-ratio stellar-

In this issue . . .

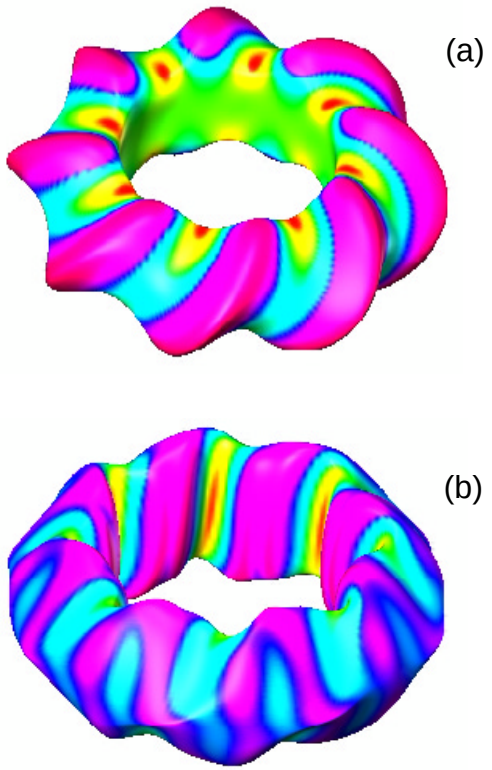

Fig. 1. Outer flux surface shape with color contours proportional to $|\boldsymbol{B}|$ magnitude for (a) an unoptimized configuration and (b) a J^*-optimized configuration.

ator configuration. We first describe our new optimization procedure and then analyze both the thermal and energetic particle transport properties of the optimized configuration. We find that sizable reductions (factors of 20–30) in thermal particle transport rates can be achieved along with a closing off of the loss cone for more energetic particles. Examination of the $|\boldsymbol{B}|$ spectrum indicates that the optimized state is neither purely quasihelical nor quasitoroidal.

Description of the Optimization Procedure

Our approach uses the VMEC three-dimensional (3-D) magnetohydrodynamic (MHD) equilibrium solver [15] as the inner physics evaluation loop of a Levenberg-Marquardt optimizer. The control variables are the shape of the outermost magnetic flux surface, which is expressed in terms of about 10 Fourier harmonics of both R and z, and the plasma current profile (in the case of stellarator/tokamak hybrids). Typically, the optimization targets used are the following: alignment of B_{min}, B_{max}, and J^* constant surfaces with magnetic flux contours; matching of $\iota(\psi)$ to a specified rotational transform profile; maintenance of a magnetic well over most of the plasma cross section; $R_0/a \approx 3$; avoidance of strongly curved segments on the flux surface; and minimization of magnetic ripple. Here B_{min} and B_{max} are the two-dimensional (2-D) functions of ψ and θ which are formed by recording the minimum/maximum value of $|\boldsymbol{B}|$ along the toroidal direction within a single field period at fixed ψ, θ. For the examples given here, the alignment of the B_{min}, B_{max}, and trapped J^* contours with ψ is typically carried out over three flux surfaces and, additionally for J^*, at four values of the pitch angle variable ε/μ. Each of the target functions is multiplied by an associated weight and summed to form a single χ^2 functional, which is to be minimized. The initial condition on the outer flux surface shape is derived from a free-boundary VMEC equilibrium based on a known set of coils.

Once a satisfactorily optimized outer flux surface is found, we vary a parameterized set of coils in order to match $\boldsymbol{B}$ at the outer flux surface [16]. In general, this is not a unique process [17] and multiple solutions are possible, depending on the number of coils per field period, the winding surface, etc. By separating the physics and coil optimizations into separate steps, efficiency is gained and a better understanding of the trade-offs of each phase of the design process is possible. We discuss only the physics (i.e., outer flux surface) optimization.

This optimization technique has been applied to an 8-field-

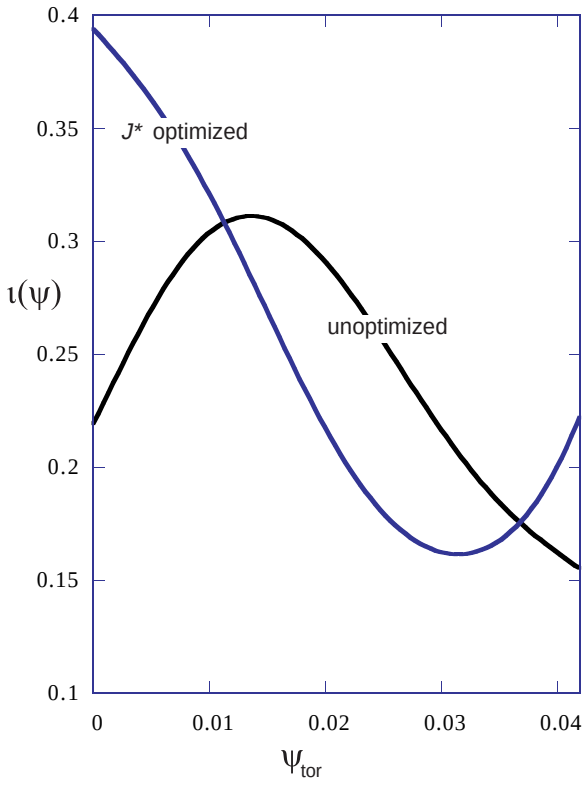

Fig. 2. Rotational transform profiles in unoptimized and J^* optimized configurations.

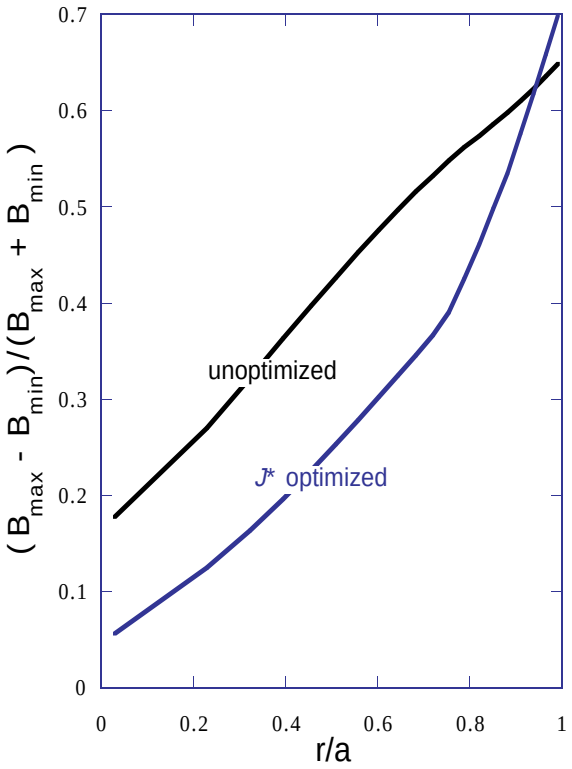

Fig. 3. Ripple strength $(B_{max} - B_{min})/(B_{max} + B_{min})$ profile for unoptimized and J^*-optimized configurations.

period, hybrid stellarator/tokamak device with major radius $R_0 = 1.4$ m, $B_{axis} = 1.2$ T, $R_0/a \approx 3$, $\langle\beta\rangle = 2\%$, and a plasma current of around 60 kA. We compare the initial unoptimized device, whose flux surface shape was determined by a set of eight external modular coils, with an optimized configuration based on the alignment of J^* with ψ. Figure 1 shows 3-D rendered flux surfaces for the two configurations with color shading to indicate the constant $|\boldsymbol{B}|$ contours.

The profiles of ι and $(B_{max} - B_{min})/(B_{max} + B_{min})$ (related to ripple strength) are shown in Figs. 2 and 3. The unoptimized case has a central region of reversed shear, while the optimized case tends to have edge reversed shear regions. The optimized case also has lower levels of ripple near the magnetic axis. In Figs. 4(a) and 4(b) the B_{min} contours show that the unoptimized configuration (a) has completely unclosed B_{min} contours (which means that all deeply trapped particles are lost), while the optimized configuration (b) has large regions of closed B_{min} contours. We have also examined the J^* contours over a range of pitch angles and find that they are more closely aligned with flux surfaces than in the original configuration.

As mentioned earlier, the J^* optimization process leads to configurations that are neither quasitoroidal nor quasi-

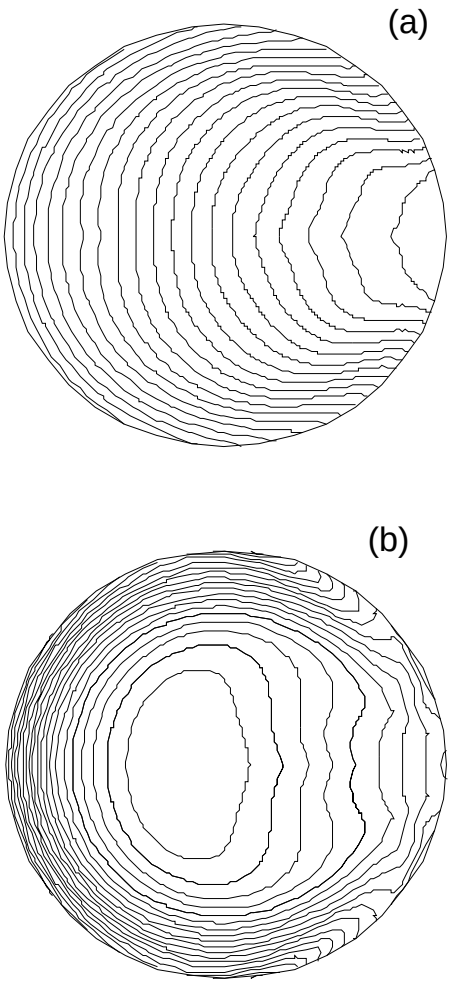

Fig. 4. B_{min} contours for (a) unoptimized and (b) J^*-optimized configurations.

helical. This is demonstrated in Figs. 5(a) and 5(b), where the B_{mn} spectra (excluding the $m = 0$, $n = 0$ mode) are plotted vs magnetic flux for (a) the unoptimized case and (b) the J^*-optimized case. Although the spread of the higher order modes has been reduced in Fig. 5(b), it still contains significant $n \neq 0$ terms and a mixture of different helicities.

The approach to bounce-averaged omnigeneity through the alignment of trapped-particle J^* surfaces with flux surfaces should be approximately equivalent to the criterion of equal angular separation between constant $|\boldsymbol{B}|$ contours on a flux surface, suggested recently in Refs. [12–14]. The differences between these criteria are of order ι/N (N = number of field periods) owing to the use of the exact J (integral along a field line) and J^* (integral along ϕ_{Boozer}) and are generally small for the configuration examined here. We have confirmed this by plotting contours of equal toroidal angle separation between a range of $|\boldsymbol{B}|$ values and find that these contours are very similar to those of the

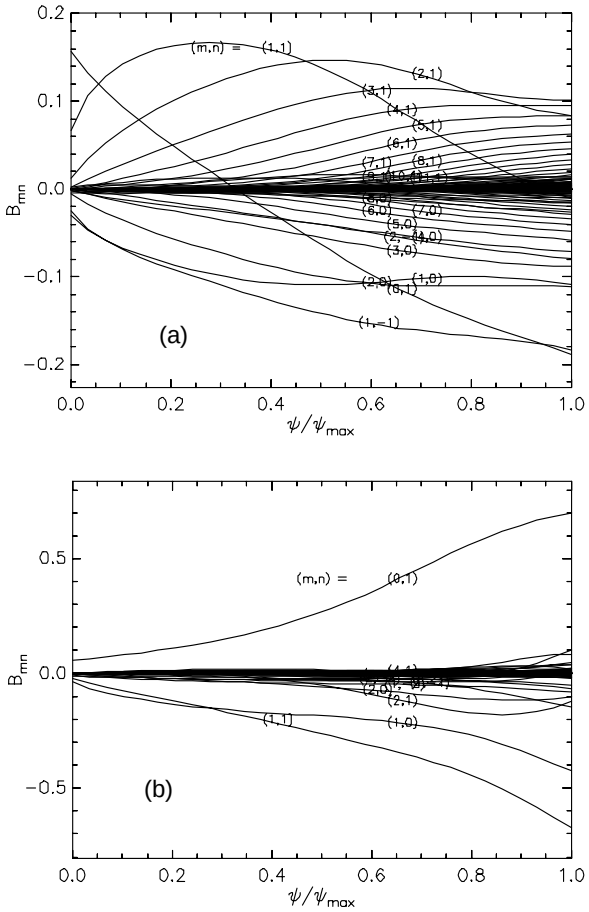

Fig. 5. B_{mn} spectrum vs toroidal magnetic flux for (a) unoptimized and (b) J^*-optimized configurations.

equivalent J^* surfaces (i.e., at $\varepsilon/\mu = |B|$).

Confinement Properties of the Optimized Configurations

Thermal Transport

In order to compare the thermal transport of the configurations presented in the previous section, we have chosen to follow the Monte Carlo evolution [18] of 256 particles started at a single radial location with a random distribution in pitch angle and in poloidal and toroidal angles and with a Maxwellian distribution in energy. The background plasma has a density of 5×10^{13} cm^{-3}, and both the background and test particle distributions have a temperature of 1 keV. The same random number seed was used for each configuration so that initial conditions are equivalent. We monitor the escape of particles and energy through the outer flux as a function of time and use this as our basic measure of thermal confinement. This loss rate has the advantage of including both the direct prompt orbit losses and diffusive losses, and it involves no assumptions regarding localized transport. A variety of other measures

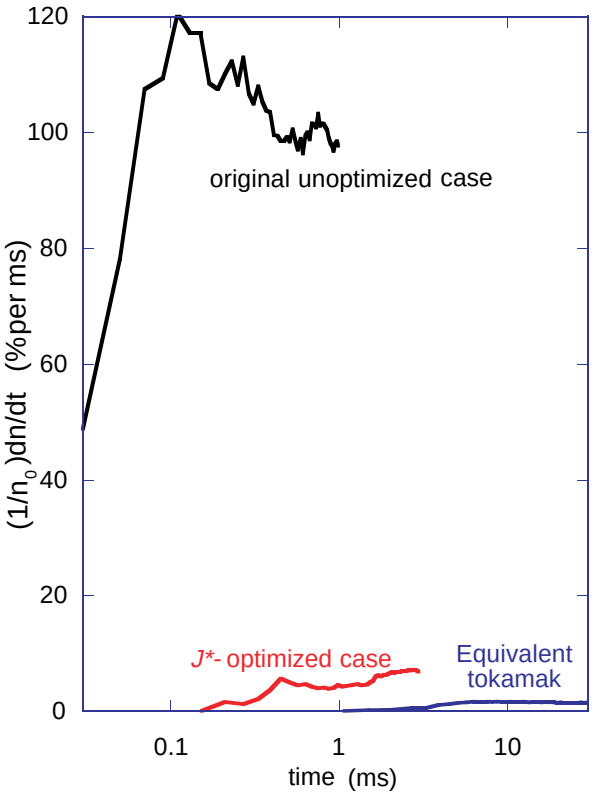

Fig. 6. Monte Carlo particle loss rates through the last closed flux surface vs time for original unoptimized configuration, J^*-optimized configuration, and an equivalent tokamak.

of thermal transport are under consideration and development.

In Fig. 6 we show the particle loss rates vs time for the original and J^*-optimized cases and for an equivalent tokamak case. The latter configuration is arrived at by taking the J^*-optimized case and retaining only the $n = 0$ harmonics. Although not all of these simulations may have reached steady state, they clearly demonstrate that the optimization procedure can substantially reduce loss rates, leading roughly to a factor of 20–30 reduction over the initial unoptimized configuration. Loss rates for the J^*-optimized case are also within a factor of 3–4 of the equivalent tokamak loss rates.

Energetic Particle Transport

The confinement of collisionless energetic particles is one of the primary motivations for the optimizations discussed here since the thermal particle confinement can, in principle, also be improved by control of the ambipolar electric field. Because most heating schemes rely on some form of energetic particle tail population, heating efficiencies can depend sensitively on the confinement of this species. As indicated in Fig. 4, the deeply trapped particles are generally promptly lost in the unoptimized configuration; as a

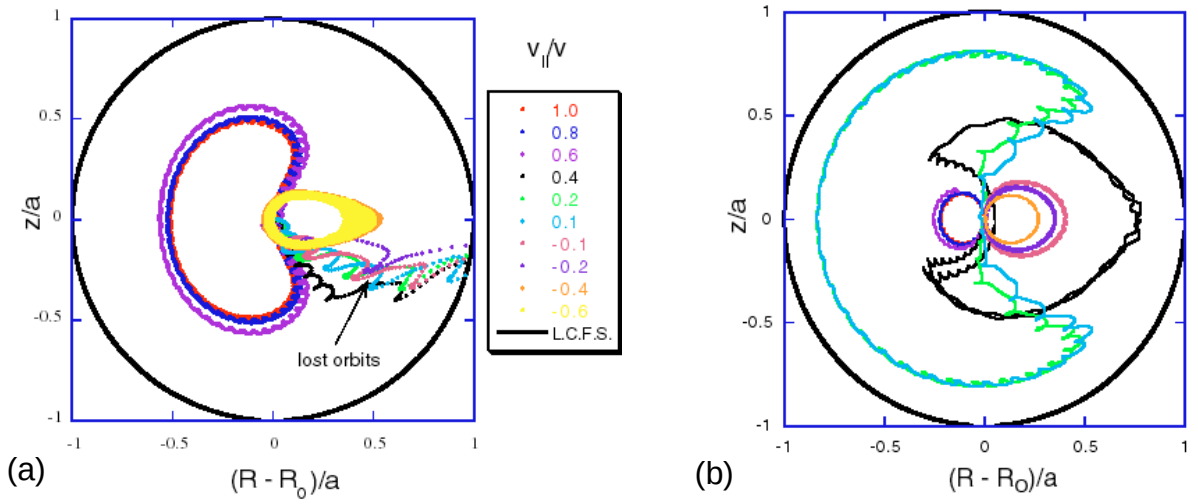

Fig. 7. Energetic 40-keV ion orbit trajectories in (a) the original unoptimized configuration and (b) the *J**-optimized configuration for orbits passing through the magnetic axis over a color-coded range of initial pitch angles ($v_{||}/v$ = –0.6, –0.4, –0.2, 0.1, 0.2, 0.4, 0.6, 0.8, 1.0).

result of the large level of ripple in these configurations, this can encompass a significant fraction of the distribution. In order to quantify this, we have followed a small ensemble of orbits at 40 keV that initially pass through the magnetic axis and have a range of pitch angles: values of $(v_{||}/v)_0$ running from –0.6 to +1 [orbits with $-1 < (v_{||}/v)_0 < -0.6$ are confined in both configurations]. More comprehensive measures of fast particle confinement are under development for these configurations. In Fig. 7 we plot the trajectories for this sample of orbits in Boozer coordinates for both the initial unoptimized configuration and the *J**-optimized configuration. The unoptimized configuration has a loss cone roughly over $-0.2 < (v_{||}/v)_0 < 0.4$. In contrast, the *J**-optimized configuration has no loss cone and confines all of the orbits shown here. In Fig. 8 we examine the confinement properties of the *J**-optimized configuration with increasing energy for a deeply trapped orbit [$(v_{||}/v)_0 = 0.1$] and a co-passing orbit [$(v_{||}/v)_0 = 1.0$] for energies

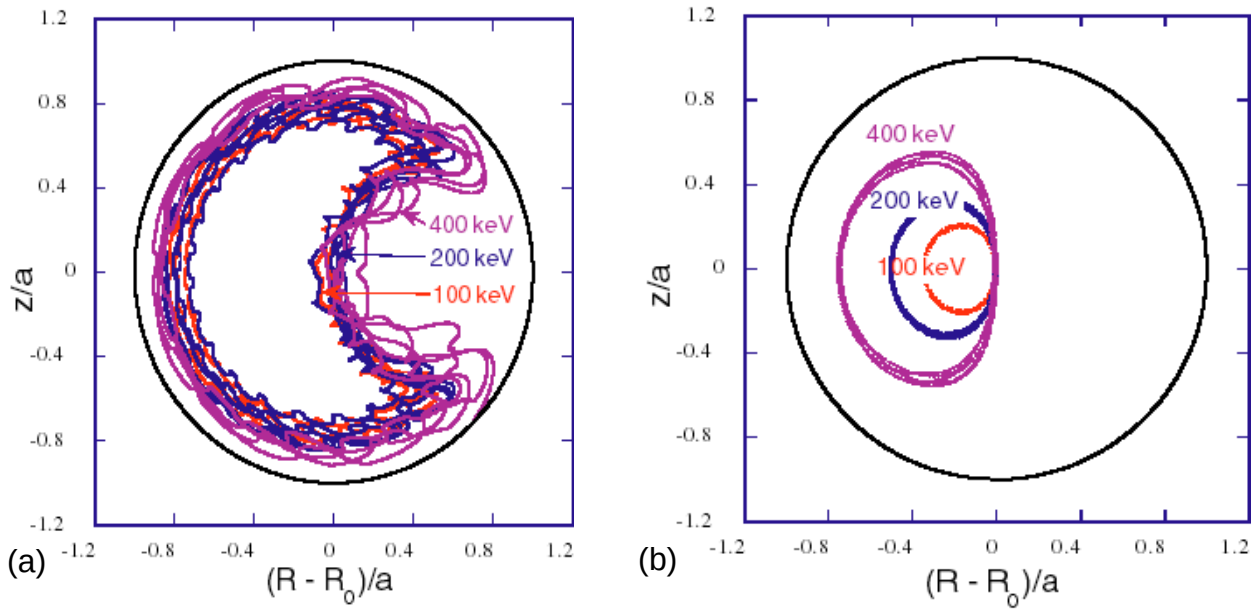

Fig. 8. Energetic ion orbit trajectories in the *J**-optimized configuration for (a) a deeply trapped $v_{||}/v$ = 0.1 case and (b) a passing $v_{||}/v$ = 1.0 case over a color-coded range of energies (*E* = 100, 200, 400 keV).

of 100, 200, and 400 keV. The deeply trapped orbit becomes lost at 400 keV, apparently because its drift per bounce has become too large to maintain J^* conservation. The passing orbits are still confined, but with significant displacements away from flux surfaces ($\Delta/a \sim 0.5$). The deeply trapped orbits show an interesting property of confined superbanana stellarator orbit trajectories in that, unlike normal tokamak banana orbits, the orbit width is essentially independent of energy (i.e., because J^* for trapped particles does not depend on energy, in the absence of electric fields). To the extent that J^* is conserved, relatively arbitrary energies will be confined on the same trajectory. The point at which J^* conservation is lost because the drift per bounce becomes too large can be extended by increasing the $\boldsymbol{B}$ field or increasing the device size.

Conclusions

We have developed a new optimization procedure for low-aspect-ratio stellarators that targets bounce-averaged omnigeneity (i.e., minimization of drift away from the flux surface) by aligning contours of the approximate second adiabatic invariant J^* with magnetic flux surfaces. This technique uses the shape of the outermost flux surface and the plasma current profile as control parameters. Our optimization has led to qualitatively new kinds of stellarator configurations that are neither quasitoroidal nor quasihelical. This additional flexibility in the $|\boldsymbol{B}|$ spectrum has opened up the available parameter space at low aspect ratio and resulted in significant improvements in confinement of both thermal and energetic particle components. We hope that such flexibility will allow the inclusion of further criteria [19] related to MHD ballooning stability as well as other potentially important physics issues. The coil reconstruction for these optimized states is relegated to a separate step and appears feasible but will require further development.

Donald A. Spong, Steven P. Hirshman, and John C. Whitson
Oak Ridge National Laboratory
P.O. Box 2009
Oak Ridge, TN 37831-8071 USA

Phone: (423) 574-1307
E-mail: spongda@ornl.gov

References

[1] B. A. Carreras, N. Dominguez, L. Garcia, et al., Nucl. Fusion **28** (1988) 1195.

[2] B. A. Carreras, V. E. Lynch, and A. Ware, *Configuration Studies of a Small-Aspect-Ratio Tokamak-Stellarator Hybrid*, ORNL/TM-13252, June 1996.

[3] D. A. Spong, S. P. Hirshman, and J. C. Whitson, Plasma Phys. Reports **23** (1997) 483.

[4] P. E. Moroz, Phys. Rev. Lett. **77** (1996) 651.

[5] D. W. Ross, P. M. Valanju, H. He, W. H. Miner, P. E. Phillips, J. C. Wiley, A. J. Wootton, and S-B. Zheng, Plasma Phys. Reports **23** (1997**)** 492.

[6] P. R. Garabedian, Phys. Plasmas **3** (1996) 2483.

[7] J. Nührenberg and R. Zille, Phys. Lett. **A129** (1988**)** 113.

[8] D. A. Garren and A. H. Boozer, Phys. Fluids B **3 (**1991) 2822.

[9] R. N. Morris, C. L. Hedrick, S. P. Hirshman, J. F. Lyon, and J. A. Rome, In *Proc. 7th Int. Workshop on Stellarators, Oak Ridge, TN, April 10–14, 1989*, IAEA, Vienna (1989).

[10] J. R. Cary, C. L. Hedrick, and J. Tolliver, Phys. Fluids **31** (1988**)** 1586.

[11] J. A. Rome, Nucl. Fusion **35** (1995**)** 195.

[12] A. A. Skovoroda and V. D. Shafranov, Plasma Phys. Reports, **21** (1995**)** 937.

[13] J. R. Cary and S. G. Shasharina, Phys. Rev. Lett. **78** (1997) 674.

[14] H. Weitzner, Phys. of Plasmas, **4** (1997) 575.

[15] S. P. Hirshman and J. C. Whitson, Phys. Fluids **26** (1983**)** 3553.

[16] S. P. Hirshman, J. C. Whitson, and D. A. Spong, "Modular Coil Design for Optimized Stellarators," in preparation.

[17] P. Merkel, J. Comput. Phys. **66** (1986) 83.

[18] R. H. Fowler, J. A. Rome, and J. F. Lyon, Phys. Fluids **28** (1985**)** 338.

[19] W. A. Cooper, Phys. Plasmas **4** (1997) 153.

First experimental results in TJ-II flexible heliac: Magnetic surface mapping

In December 1996 a short campaign of magnetic surface measurements was carried out in the flexible Heliac TJ-II, a medium-size device (R = 1.5 m, $\langle a \rangle$ = 0.2 m, B_0 = 1.0 T) located at CIEMAT (Madrid). A limited number of configurations was studied with the primary goal of checking the high accuracy required in the positioning of the coils and the vacuum vessel [1].

Initial measurements of the magnetic surfaces were made using a directed electron beam in combination with a movable fluorescent rod array [2–7] before the final adjustment of the toroidal field (TF) coils. Therefore, the maximum deviation of some of these coils with respect to the nominal position (2.9 mm, in the radial direction) exceeded the design tolerance (1 mm). The magnetic field was steady state, B_0 = 0.05 T (5% of the nominal field), with 50-s pulses. The technique is based on imaging the spots produced by the impact of an electron beam, launched in the vacuum vessel along the magnetic field lines, that intersects an array of four fluorescent rods (1.5 mm diam each, coated with P24, ZnO:Zn powder), sketched in Fig. 1, that sweeps the vessel cross section.

The electron beam (0.5 mm diam at the gun exit; energy 150 eV) is launched with the main velocity component, $v_{||}$,

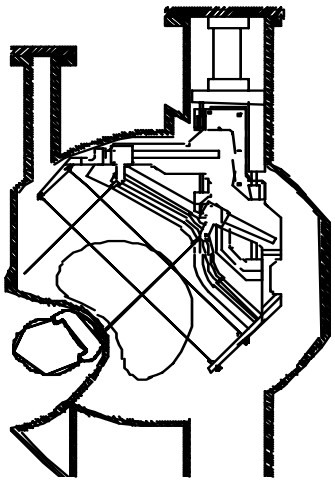

Fig. 1. Schematic of the fluorescent detector.

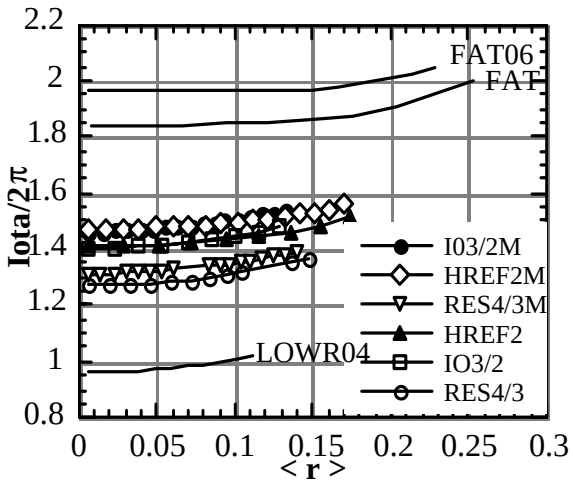

Fig. 2. Theoretical rotational transform profiles of the measured configuration.

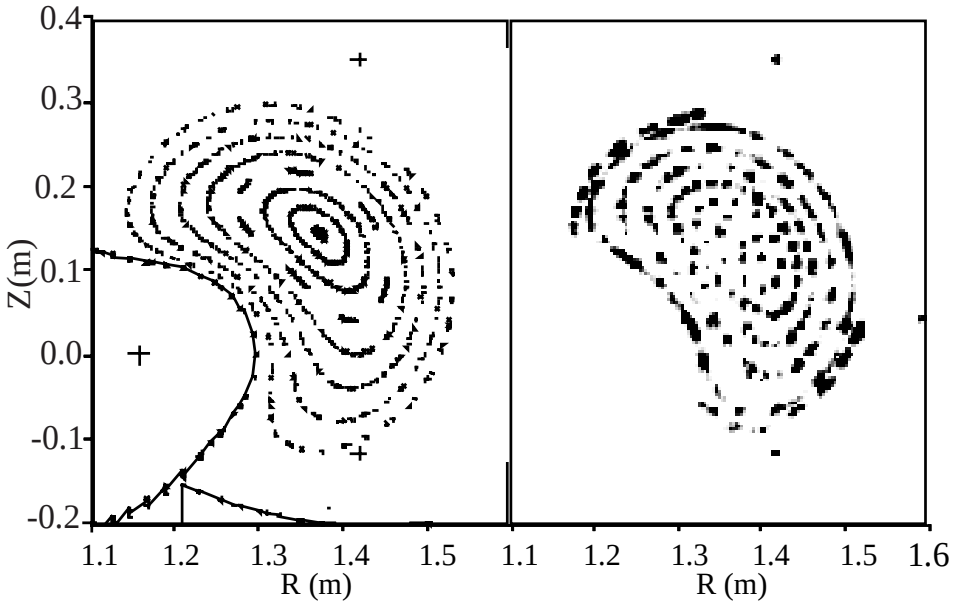

Fig. 3. Calculated TJ-II flux surfaces (left) compared to those measured using the fluorescent detector (right).

parallel to the magnetic field of the device. The gun head is driven over a rectangular region (147 mm in the radial direction, 328 mm in the vertical direction) by means of a PLC-controlled manipulator installed in a top port; the magnetic surfaces are measured about 199° away in the toroidal direction. Three LEDs located inside the vacuum vessel, at the same cross section where the image is formed, are used as a reference system for measuring distances. The images are acquired with an intensified CCD camera, looking perpendicularly to the image plane through a tangential NBI port, and processed by means of an image integrator. The spatial resolution of the experimental system is estimated to be about 2 mm (each fluorescent rod is 1.5 mm thick, plus the space charge broadening of the electron beam cross section as it travels around the torus).

TJ-II configurations are low shear. Nine of them have been measured, covering the rotational transform range $0.96 \leq \iota \leq 1.97$. Their iota profiles are shown in Fig. 2. In all the studied configurations, closed and nested magnetic surfaces are found, provided that the low-order resonances (ι = 1, 3/2, and 2, in our case) are kept away from the corresponding rotational transform profile. The size and shape of the magnetic surfaces, as well as the coil current values needed for all the configurations, fully agree with the design parameters. Figure 3 shows that the calculated and experimental flux surfaces for the standard configuration, named HREF2 (ι = 3/2), are in very good agreement. If the ι = 3/2 value is allowed inside this low-shear configuration, islands are measured, probably due to the above-mentioned uncorrected internal field error, in good qualitative agreement with the theoretical model. After final positioning of the TF coils within the design tolerances, additional experiments will be performed to further investigate this point.

The TJ-II Team
Asociación Euratom-Ciemat para Fusión
Av. Complutense 22, 28040
Madrid, Spain

Phone: +34-1-346.6159
E-mail: Carlos.Alejaldre@ciemat.es

References

[1] The TJ-II Team, 24th EPS Conference, Berchtesgaden, Germany (1997).

[2] H. Hailer et al., in Controlled Fusion and Plasma Physics (Proc. 14th Eur. Conf. Madrid, 1987), **11D**, Part I, European Physical Society (1987) 423.

[3] R. Jaenicke et al., Nucl. Fusion **33** (1993) 687.

[4] G. G. Lesnyakov et al., Nucl. Fusion **32** (1992) 2157.

[5] H. Lin et al., Rev. Sci. Instrum. **66** (1995) 464

[6] M. Shats et al., Nucl. Fusion **34** (1994) 1653.

[7] E. Ascasíbar et al., Nucl. Fusion **37** (1997).

Design and construction of the SC current transmission system for the LHD

The Large Helical Device (LHD) is a heliotron configuration intended for fusion research. It includes a pair of helical superconducting (SC) coils (H1 and H2) and three sets of poloidal SC coils (IS, IV, and OV). Each helical coil consists of three block coils that can be excited independently. Therefore, nine SC bus lines are necessary: six for the helical coils and three for the poloidal coils. The maximum operating current of the SC coils is 31.3 kA for the outer vertical field coils, OV. The average distance between the SC coils and their power supply system is about 55 m. We decided to use an SC current feeder system for LHD considering the following advantages:

- reduction of the power supply capacities,
- simplification of the bus line assembly process on site, and
- space saving around the main device.

In the case of LHD, the electrical power consumption exceeds 1.5 MW. To develop an SC current transmission system, a full scale model of a 20-m-long SC bus line was fabricated in 1994. Experiments were conducted to study the characteristics of this full-scale model. The design of the actual SC current transmission system for LHD is based on these experimental results.

Figure 1 shows a bird's-eye view of the SC current transmission system for LHD. The design concepts for the system are as follows: (1) Fully stabilized SC properties should be satisfied when a rated current of 31.3 kA (for OV coils) flows. (2) The breakdown voltage of the current

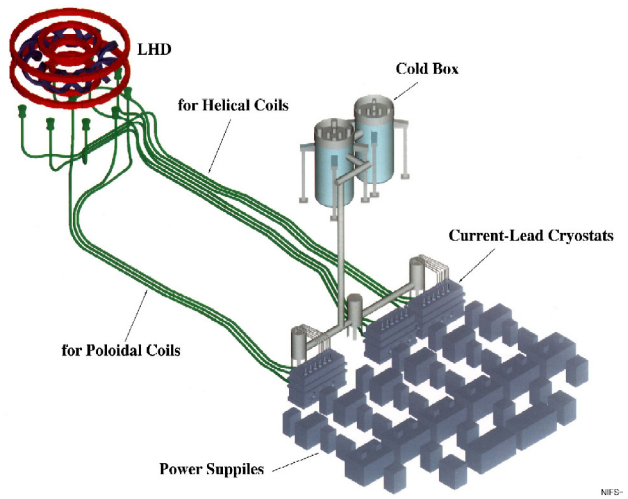

Fig. 1. Bird's-eye view of the SC current transmission system for LHD.

transmission system should be higher than that of the SC coils. (3) The system should be able to maintain its rated current-carrying capacities for 30 minutes, even when the supply of coolants to the current feeder system is interrupted.

The SC current transmission system requires excellent reliability and safety, exceeding that of the SC coils of LHD, because the stored magnetic energy of the coils must be discharged through the SC bus lines when the coils quench.

The internal structure of a flexible SC bus line is shown in Fig. 2. An aluminum-stabilized, SC-compacted stranded cable was specially developed to satisfy the high stability and flexibility requirements. Electrical insulation was inserted between a pair of +/- cables. The vacuum-insulated transfer line consists of five corrugated stainless steel tubes assembled coaxially. A pair of SC cables is covered with insulation layers to satisfy the requirements for electrical insulation between the cables and the surrounding corrugated tubes. Liquid helium flows through the innermost channel to the peripheral terminal and then returns through a second inner channel as two-phase helium. The fourth channel is the 80 K helium gas channel, and the third and fifth channels are vacuum insulation spaces.

The construction of the actual SC bus lines for LHD was started in FY 1995, and their installation on site began in early 1997. Figure 3 shows the release of the SC bus line from the cable drum. The SC bus line must be flexible because the installation routes from the coils to their power supplies have bends as shown in Fig. 1. The minimum bend radius is determined to be 1.5 m, because of legal restrictions on the height, width, and other parame-

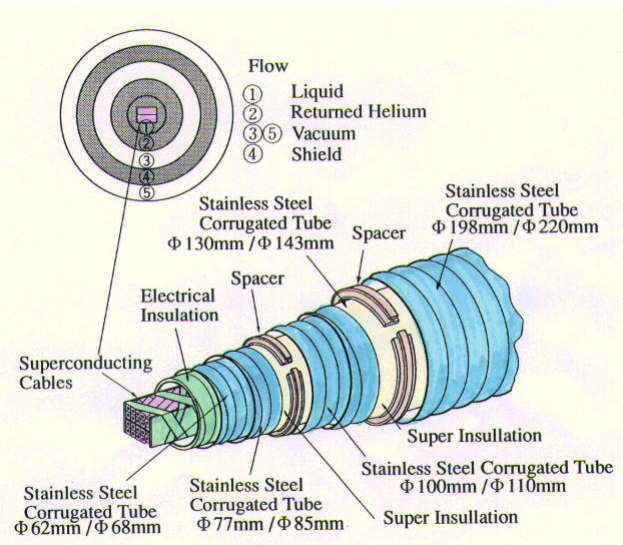

Fig. 2. Internal structure of a flexible SC bus line.

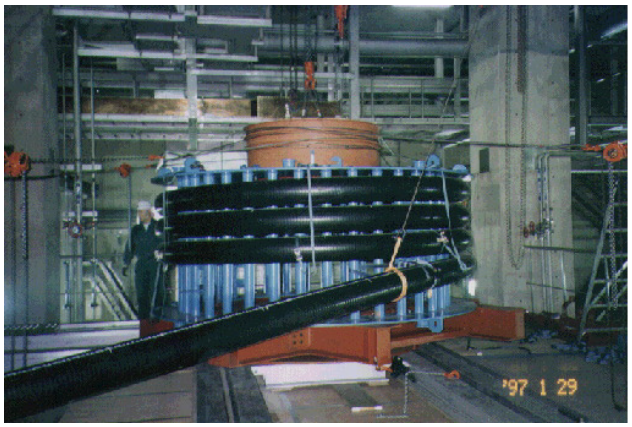

Fig. 3. Releasing the SC bus line from the cable drum.

Fig. 4. Tentative placement of nine SC bus lines beneath the LHD main hall.

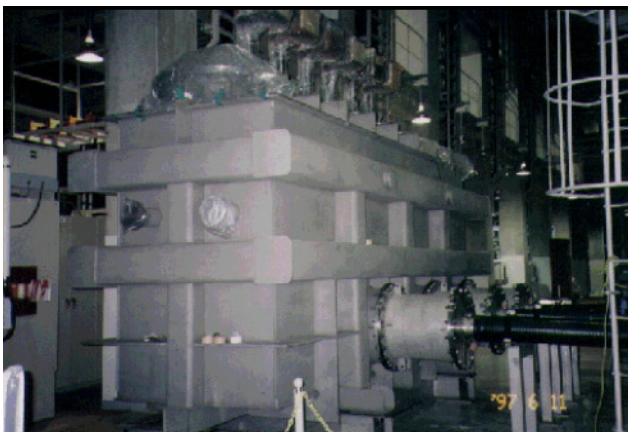

Fig. 5. Installation of a current-lead cryostat for the helical coils.

ters of traffic regulation in Japan. Nine bus lines have been installed in the experimental building. The tentative fixations of nine SC bus-lines below the LHD main hall are shown in Fig.4.

The total length of the SC bus lines is 497 m, and the current carrying capacity of each SC bus-line is 160 MW. The length and transmission capacity of the SC bus lines are the largest scale in the world, and the construction of these current transmission systems is a pioneering achievement. Already, one current-lead cryostat has been installed near the power supply system, as shown in Fig. 5. The other two current-lead cryostats will be prepared this year.

Shuichi Yamada for the LHD team
National Institute for Fusion Science
Oroshicho, Toki 509-52, Japan

E-mail: yamadas@LHD.nifs.ac.jp

Construction of the cryogenic system for the LHD

The cryogenic system for the Large Helical Device (LHD) is now in its final stages of assembly. This system consists of the helium refrigerator/liquefier, the LHD cryostat, and the peripheral equipment, such as superconducting (SC) bus lines, control valve boxes, cryogenic transfer tubes, etc. Figure 1 shows the main parts of the LHD cryogenic system: the LHD cryostat, which contains the SC helical coils, the poloidal coils and the coil supporting structures; the helical and poloidal valve boxes by which the flows of cryogen from the He refrigerator to the helical and poloidal coils are controlled; and the cold box of the He refrigerator. The He refrigerator is separated from the LHD cryostat by a 2-m-thick concrete wall, they are connected by multiple-line transfer tubes routed through the basement to allow radiation shielding in phase II operations.

Safe and stable operation of the SC coil system is required because the total magnetic stored energy of the LHD will be 0.9 GJ in phase I operations and 1.6 GJ in phase II operations. Reliable long-term operations are necessary for the cryogenic system because a warm-up of the total system, including the SC coils, will be done only once or twice a year. Three different cooling schemes are used for each cooling object: pool boiling for the helical coils (cold mass of 240 tons), forced flow of supercritical helium for the poloidal coils (182 tons), and forced flow of two-phase helium for the coil supporting structure (390 tons) and the SC bus lines (total length of 463 m). Figure 2 shows the flow diagram for the cooling objects of the LHD cryogenic system. In steady-state operation, there are four kinds of

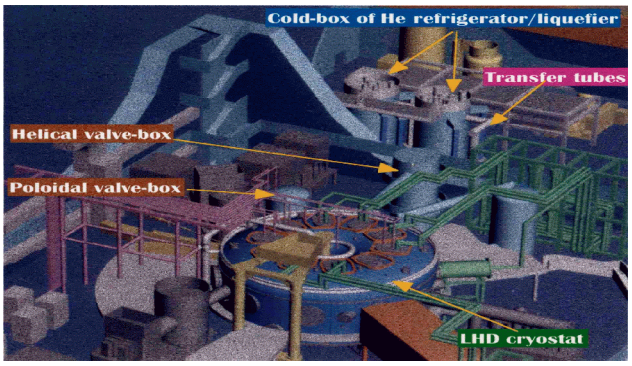

Fig. 1. A bird's-eye view of the main parts of the LHD cryogenic system.

cryogen: (1) supercritical helium for the poloidal coils, (2) two-phase helium for the coil supporting structure and the SC bus lines, (3) liquid helium for the helical coils and the current leads, and (4) 40–80 K gaseous helium for the thermal radiation shields of the LHD cryostat, the helical and poloidal valve boxes, the current-lead cryostat, and the multiple-line transfer tubes.

The helium refrigerator/liquefier has cooling capacities of 5.65 kW at 4.4 K, 20.6 kW from 40 K to 80 K and 650-L/h liquefaction. Shown in Fig. 3 are the main components in the He refrigerator room: the cold box, the helium gas purifier, the 20,000-l liquid helium reservoir, and the 50,000-l liquid nitrogen reservoir, which is used only for the initial cooldown and for the helium purifier. The cold box is divided into two stages of temperature because of a size limit for land transportation. Eight oil-injected screw compressors are installed in the compressor room, which is 50 m away from the He refrigerator room, and they are connected with pipes running in an underground tunnel.

The development of a new control system, which employs highly flexible and expandable hardware and software, is crucial for the LHD cryogenic system because of its fairly

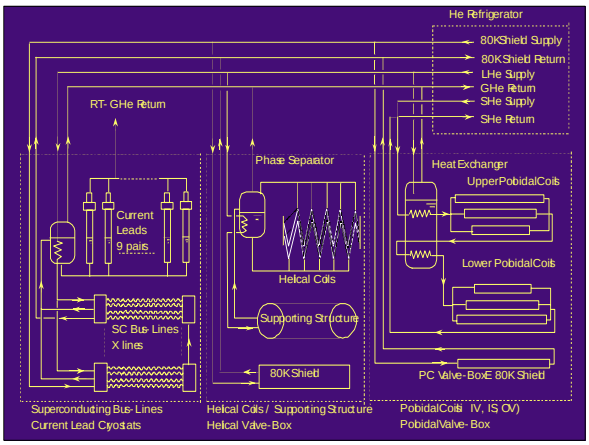

Fig. 2. Flow diagram for the cooling objects of the LHD cryogenic system.

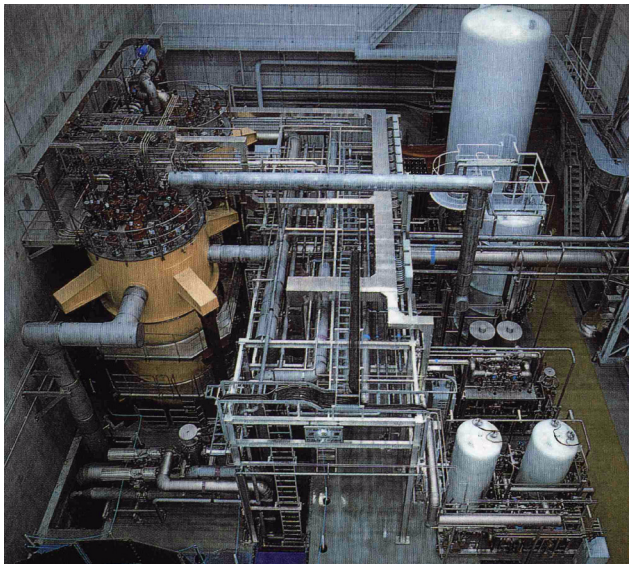

Fig. 3. The main components of the helium refrigerator/liquefier.

complicated cooling schemes. As shown in Fig. 4, the cryogenic control system consists of workstations, VME (Versa Module Europe) controllers, local area networks (LANs), operating graphic consoles, peripherals, and signal terminals. The control system is set up as a redundant system, which significantly improves operational reliability with fault diagnosis of each component. The overall control system can be expanded using standard hardware and operating software. Furthermore, software tool packages based on these standard items are being developed to provide us with the ability to construct flexible control programs easily. These software tool packages have the advantages of system configuration, easy creation of graphic control panels, and easy programming of sequence and loop control.

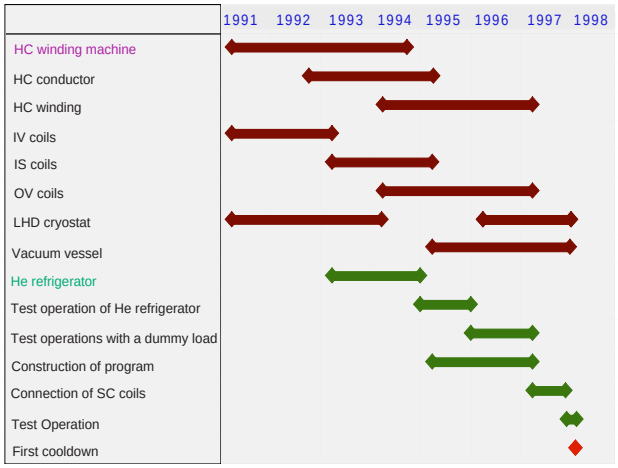

Fig. 5. Construction schedule of the LHD cryogenic system.

Figure 5 shows the construction schedule for the LHD cryogenic system. The engineering design and construction of the helium refrigerator/liquefier was started in 1992 and completed at the end of 1994. A series of commissioning runs was successfully completed and various design performances levels were confirmed. Then we conducted test operations of the helium refrigerator/liquefier with a dummy load, which can simulate the heat load of the LHD, to gather data on the cooling characteristics of a large-scale cryogenic system. The assembling of the LHD cryogenic system is now at the final stage and will be completed at the end of 1997. The first cool-down of the LHD is scheduled at the beginning of 1998.

Toshiyuki Mito for the LHD team
National Institute for Fusion Science
Oroshicho, Toki 509-52, Japan
E-mail: mito@LHD.nifs.ac.jp

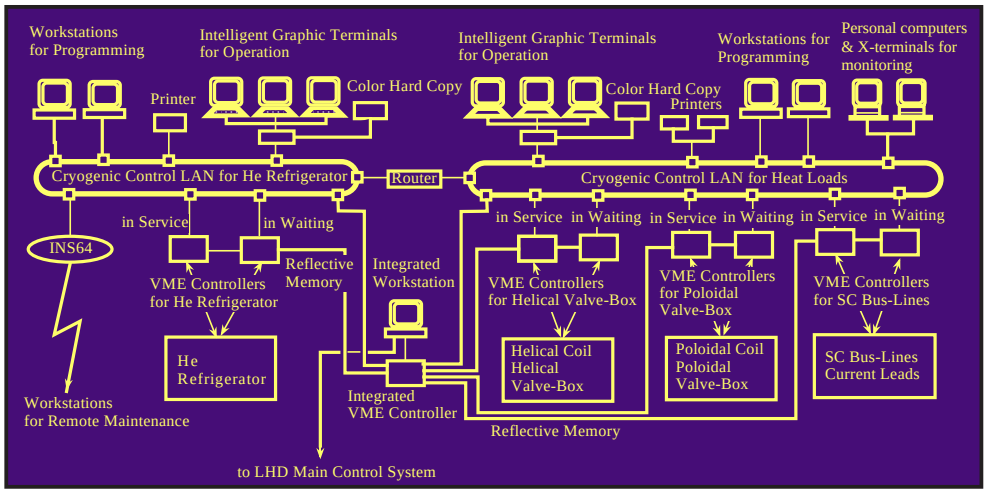

Fig. 4. Cryogenic control system for the LHD.

Cornerstone placed for the Greifswald branch of IPP Garching

The cornerstone for the laboratory buildings of the Greifswald Branch of IPP Garching was placed (Fig. 1) at the site of the new institute for the advanced stellarator Wendelstein 7-X (W7-X) on 19 June 1997. About 300 guests participated in this ceremony.

After the welcome speech by K. Pinkau, addresses were delivered by the Prime Minister of the Land Mecklenburg-Vorpommern and by its Minister on Cultural Affairs; by high-level politicians of the German Federal Ministry of Research and Education, of the European Commission, and of the City of Greifswald and its University; and by the President of the Max Planck Society.

This ceremony formally initiates the construction work for the experimental hall and the associated buildings of W7-X (Fig. 2). The mission of this experiment is to demonstrate, without the use of tritium, the particularly beneficial properties of advanced stellarators for the development of a future economical fusion power station. As a reminder, the basic components of W7-X are:

- Cryostat composed of 5 modules,
  helical plasma axis,
  ~240 ports/penetrations
- Superconducting magnet system,
  50 modular coils (nonplanar, $B_0 = 3$ T, stored energy 610 MJ),
  20 TF coils (planar, field variation)
- Divertor (actively cooled for steady-state operation),
  3-D target plates (20 m^2, design load 10 MW/m^2),
  baffle plates (30 m^2, low-Z material),
  wall protection (~200 m^2, carbon tiles),
  cryopumps (10×15000 l/s, He-pumping),
  control coils (power distribution, normal conducting)
- Plasma heating systems
  ECRH (10×1MW, 140 GHz, stationary operation),
  ICRH (2×2 MW,
  NBI (3– to 4,5-MW H^0 / D^0 during first stage of experimental operation,
  pellet injection (optional)
- Power supply system (110 kV, 20 kV)
- Plasma diagnostics and data acquisition

The Greifswald Branch of IPP Garching will eventually comprise about 90 scientists and 200 engineers and technicians in three divisions. The founding director of the Greifswald Branch is G. Grieger. At present, the Stellarator Physics Division (headed by J. Nührenberg) is housed in rented offices in downtown Greifswald. This group is connected via high-speed data links to IPP Garching. Two W7-X Experimental Divisions will be established subsequently at Greifswald.

In parallel to the building activities for the Greifswald Branch, activities for construction of the W7-X experiment are being pursued at Garching. The R&D for the basic machine is being done by the W7-X Construction Team (headed by M. Wanner), and preparation for W7-X heating by the IPP Technology Division (headed by R. Wilhelm). Both activities are in close cooperation with other institutions and industry. Development of the plasma diagnostics for W7-X is a task of the Garching Experimental Division E3 (headed by F. Wagner), whose main activity is the operation of the W7-AS experiment. The Garching Experimental Division E2 (headed by G. Grieger) is concentrating on the R&D of the W7-X diver-

Fig. 1. G. Grieger, the founding director of the Greifswald Branch Institute of IPP, closes the cover plate of the W7-X cornerstone.

Fig. 2. Model of the Greifswald Branch Institute, showing the experimental hall for W7-X and ancillary buildings (at left) and the three laboratories and the center building (at center and right).

tor and the extrapolation of W7-X towards a future stationary fusion power station, the Helias Reactor, HSR.

F. Rau for the W7-X Team
EURATOM- Association
IPP Garching, Germany

E-mail: ffr@ipp-garching.mpg.de

Recent Helias reactor study developments

Introduction

Helias (Helical Advanced Stellarator) configurations have been developed at IPP Garching as the basis for the Wendelstein 7-X experiment (W7-X), which is now under construction in Greifswald. The basic physical features of a Helias configuration are its capability to confine an MHD-stable plasma up to average beta $\langle\beta\rangle = 5\%$, low neoclassical losses which are not prohibitive to ignition, and good confinement properties of highly energetic alpha particles. The Helias reactor, HSR, is an extrapolation of the W7-X configuration to reactor dimensions, with some minor modifications to improve the confinement of highly energetic alpha particles. A summary of the Helias reactor studies was presented at the IAEA conference in Montreal in October 1996 [1]. The recent developments mainly concentrate on the reduction of the magnetic field in order to permit the technical realization using NbTi superconductors and the issue of mechanical stresses. Physics studies are focused on finite-beta equilibria, ignition scenarios, and alpha particle confinement.

Coil system

The coil system of the HSR consists of 5 field periods with 10 coils per period. In contrast to a previous design, the magnetic field on the coils has been reduced by using a trapezoidal shape for the coil cross section and by reducing the average field by 5%. The winding pack is split into two parts in order to reduce the overall current density at the location of maximum magnetic field. Because of this modification, the maximum field on the coils is now 10 T, which is in the range of NbTi technology at a temperature of 1.8 K. Furthermore, slight modifications of the coil geometry have been made to provide the necessary space for blanket and intercoil support elements. Each coil is enclosed in a steel case, which is designed as a box-type profile with a central web for mechanical stiffening (see Fig. 1). The minimum bending radius of the superconducting cable is 1.4 m. Force and stress analyses of the Helias coil system are reported in Ref. [2]. An optimized design of the intercoil support system is in progress.

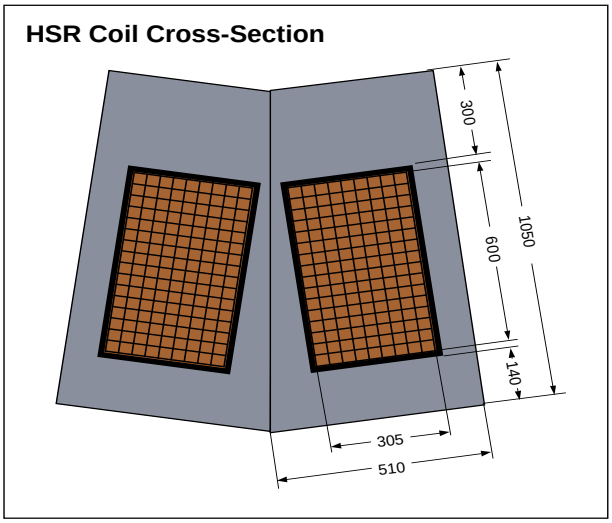

Fig. 1. Cross section of a modular coil.

Table 1. Parameters of the HSR coil system

Major radius	22	m
Number of coils	50	
Average coil radius	5	m
Max. field on coils	10	T
Total magnetic energy	100	GJ
Weight of one coil	300–350	tonnes
Windings per coil	288	
Current in winding	37.5	kA
SC winding pack per coil	80	tonnes
Current density	29.5	$MA \cdot m^{-2}$

Finite-beta equilibrium

The magnetic field of a finite-beta equilibrium is computed iteratively using the free-boundary equilibrium code NEMEC [3] inside the last magnetic surface and the code MFBE [4] outside the plasma. Starting from a vacuum field with inward-shifted magnetic surfaces, a finite-beta equilibrium with $\langle\beta\rangle = 5\%$ was computed. A vertical field of 0.04 T is provided by the modular coils and compensates the Shafranov shift at the outermost surfaces. As can be seen from Fig. 2, there is a finite Shafranov shift; however, the radiating plasma center is still centered with respect to the first wall, thus avoiding large hot spots from neutron irradiation. The Shafranov shift is in the expected range for Helias configurations. The effective plasma radius shrinks slightly at finite beta, leading to a modification of the island region at the boundary. There is also a reduction of the rotational transform (ι) profile as seen in Fig. 3. The remnants of the $\iota = 1$ islands determine the pat-

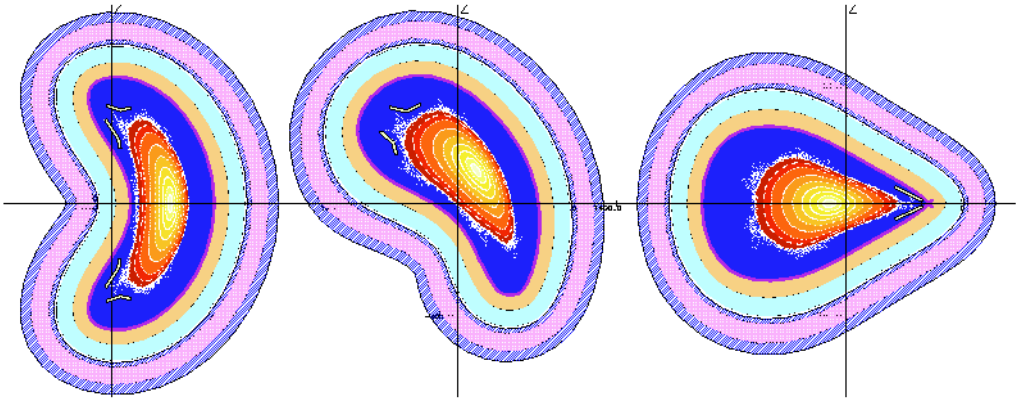

Fig. 2. Cross sections of plasma and coils at ⟨β⟩ = 5% and toroidal angles of 0, 18°. and 36°, respectively. The radial width of blanket and shield is 1.3 m at all locations around the torus.

tern of plasma flow to the divertor plates. As shown by Monte Carlo calculations of particle orbits (Fig. 2), divertor target plates collect the outstreaming plasma. The finite-beta plasma at ⟨β⟩ = 5% is stable according to both Mercier and resistive interchange criteria. It is expected that the ballooning limit is also in this range.

Neoclassical transport

The neoclassical transport characteristics of the new HSR configuration are very similar to those of its predecessors. To summarize, the vacuum magnetic field has an effective helical ripple (for 1/ν transport) of 2.5% or less over the entire plasma cross section. Neoclassical electron losses are thereby small enough to allow ignition even for the "ion root" solution of the ambipolarity constraint. This is a critical point, as the envisaged plasma parameters do not allow operation at the more favorable "electron root." Finite plasma pressure introduces two transport-relevant

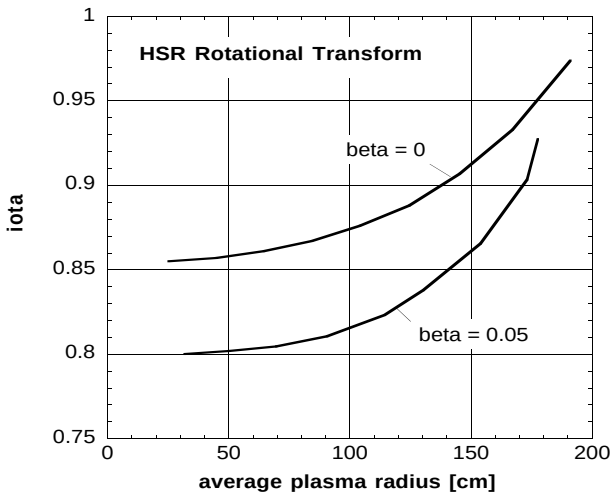

Fig. 3. Profile of rotational transform ι at ⟨β⟩ = 0 and 5% (lower curve).

changes in the magnetic field spectrum: the reduction of the mirror term on the magnetic axis and a significant radial variation of the flux-surface-averaged value of *B*. The first is a relatively modest effect and actually reduces the effective helical ripple to 2% or less by means of improved drift optimization. The second is critical for the confinement of highly energetic alpha particles but is of only minor importance for bulk plasma transport.

Alpha particle studies

Confinement of trapped alpha particles is a critical issue in HSR. However, finite plasma pressure produces a true minimum-B configuration in which the majority of reflected alpha particles are confined for at least one slowing-down time [5]. Nevertheless, modular coil ripple leads to a small fraction of "very prompt" losses (with confinement times less than 10^{-3} s), potentially resulting in "hot spots" on the first wall of the reactor. To estimate the severity of the problem, the alpha particle birth profile is combined with the fraction of phase space in which the birth takes place in a modular ripple. For the ⟨β⟩ = 5% case, the total heat load on the first wall due to very prompt losses is estimated to be less than 2.2 MW. Thus, the power loss caused by these alpha-particles is negligible. However, future investigations must clarify the magnitude of the power density on the first wall is and whether local destruction might occur. Ash accumulation of thermal alphas is another issue to be studied; presently a fraction of not more than 5% thermal alphas is assumed. If the fraction of thermal alphas is higher, the dilution effect becomes too pronounced for ignition.

Ignition scenarios

The ignition phase of the HSR has been computed using the 1-D time-dependent ASTRA code [6]. The transport model uses the neoclassical model including the nondiagonal transport coefficients and the anomalous thermal conduction corresponding to ASDEX L-mode scaling. The

radial electric field results self-consistently from the ambipolar condition. In the envisaged parameter regime, with axis values $T(0) = 14$ keV and $n(0) = 3 \times 10^{20}$ m^{-3}, the ion root determines the electric field. Fuelling of particles is provided by D-T pellet injection. The results of the computations show that ignition can be achieved within 10 seconds using a net heating power of 70–80 MW. Typical confinement times of steady-state operation are 1.6–1.8 s, which coincides very well with the predictions of Lackner-Gottardi scaling. A critical parameter is the fraction of cold alpha particles which must not exceed 5–6%. Results of the ASTRA code are summarized in Ref. [7].

Another approach to ignition is the extrapolation on the basis of empirical scaling laws [8] which are deduced from the international stellarator data base. On the basis of the International Stellarator Scaling (ISS, which averages over all stellarator systems) ignition cannot be achieved; an improvement factor for the confinement time is needed. However, Lackner-Gottardi scaling and the W7-AS scaling, which describe the data in Wendelstein 7-A and Wendelstein 7-AS, predict ignition without any improvement factor (Fig. 4).

Table 2. Plasma parameters in a Helias reactor

Major radius	22	m
Average plasma radius	1.8	m
Field on axis	4.75	T
Temperature T(0)	14	keV
Average temperature	4.9	keV
Electron density n(0)	3.15	10^{20} m^{-3}
Max. beta	15.6	%
Average beta	4.6	%
Alpha power	608	MW
Fusion power	3040	MW
Confinement time τ_E	1.8	s
Fraction of alpha particles	5	%

The wall loading by 14-MeV neutrons has been computed taking into account the geometry of the finite-beta plasma. Consistent with the data in Table 2 the peak neutron wall load is 1.6 MWm^{-2} and the average value 0.8 MWm^{-2}. In the region of the divertor plates (see Fig. 2) radiation by fast neutrons is rather weak at about 0.6 MWm^{-2} (Fig. 5).

Conclusions

First results of finite-beta-equilibria computations in HSR have verified that the Shafranov shift at $\langle\beta\rangle$ =5% is acceptable and that neutron emission is distributed equally to the inboard and outboard sides. The magnetic field has been reduced slightly from that in previous concepts to accommodate the requirements of NbTi superconductor. Ignition in the HSR can be achieved on the basis of empirical scaling from present-day stellarator experiments; assumptions about improvement factors are not needed.

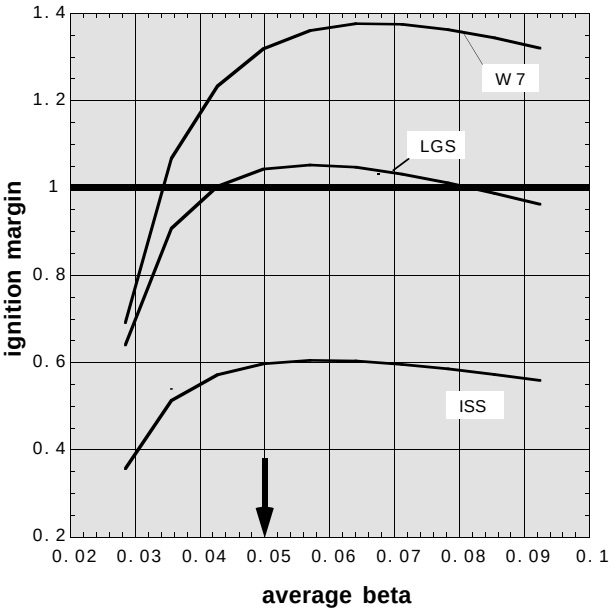

Fig. 4. Ignition margin of HSR using various scaling laws.

Data on the HSR have been included in a recent study on the economic viability of fusion power by Hender et al. [9]. Extrapolating the costs of ITER to fusion power plants, the authors conclude that the cost of electricity (COE) in a Helias reactor is very similar to that in a tokamak reactor, when an equivalent level of physics and technology advance is assumed. This result shows that in spite of the large aspect ratio, Helias reactors are competitive as fusion power plants.

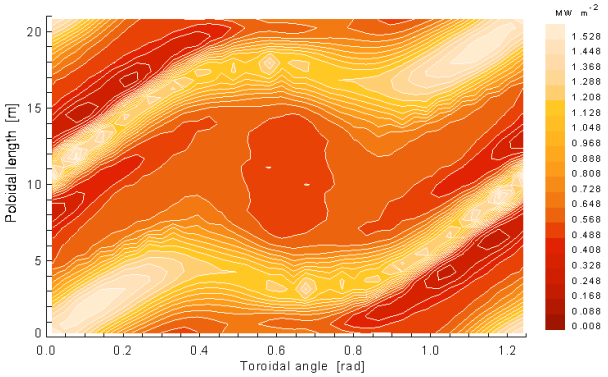

Fig. 5. Power deposition of 14-MeV neutrons on the first wall. One field period, the vertical axis is the poloidal length in meters.

References

[1] C. D. Beidler et al., presented at the 16th IAEA Fusion Energy Conference, Montreal, Oct. 1996, paper CN-64/G1-4.

[2] E. Harmeyer, N. Jaksic, and J. Simon-Weidner, in 19th Symposium on Fusion Technology, Lisbon 1996.

[3] S. P. Hirshman, W. R van Rij, and P. Merkel., Comput. Phys. Commun. **43** (1986) 143–155.

[4] E. Strumberger, Nucl. Fusion **37** (1997) 19.

[5] W. Lotz et al., Plasma Phys. Controlled Fusion, **34** (1992) 1037.

[6] G. V. Pereverzev et al., IPP report 5/42 (1991).

[7] N. Karulin, IPP report 2/337 (1997).

[8] U. Stroth, M. Murakami, R.A. Dory, H. Yamada, S. Okamura, F. Sano, and T. Obiki, Nucl. Fusion **36** (1996) 1063.

[9] [9] T. C. Hender, P. J. Knight, and I. Cook, Fusion Technol. **30,** No 3, Part 2b (1996) 1605.

C. D. Beidler, G. Grieger, E. Harmeyer, F. Herrnegger, J. Kisslinger, E. Strumberger, H. Wobig, A.V. Zolotukhin
Max-Planck-Institut für Plasmaphysik
EURATOM-Association
Garching bei München, Germany

N. Karulin
Nuclear Fusion Institute
Moscow, Russia

E-Mail: how@ipp-garching.mpg.de

Second Announcement and Final Call for Papers

Joint Conference: 11th International Stellarator Conference & 8th International Toki Conference on Plasma Physics and Controlled Nuclear Fusion (ITC-8),"Helical System Research"

September 29–October 3, 1997, Toki, Japan

The International Toki Conference on Plasma Physics and Controlled Nuclear Fusion has been held annually at Toki. A selected topic in plasma physics and fusion engineering is discussed each year. The International Stellarator Conference is held every two years, and the next conference is scheduled to be held in Japan. These two conferences will be held as a joint conference in Toki; the topic will be helical system research.

Topics: The Joint Conference of 11th International Stellarator Conference and 8th International Toki Conference will focus on Helical System Research. This conference covers

- Confinement-related experiments and relevant theories: L-mode, H-mode, high-T_i mode, effect of radial electric field
- New devices, advanced helical concepts, reactor studies
- Steady-state operation: physics and technology related to particle and energy balance

The program consists of invited papers, oral presentations, and poster presentations.

Date and place: The Conference will be held September 29–October 3, 1997 at Ceratopia Toki Conference Hall in Toki, near Nagoya. On September 29, the registration desk will be open from 16:00 to 18:00.

Detailed information, registration forms, paper formats, etc. can be found on the Conference Web site:

http://www.nifs.ac.jp/~itc8/

or by contacting the conference secretary:

Dr. S. Sudo
National Institute for Fusion Science
322-6, Oroshi-cho
Toki, 509-52 Japan

FAX: 81-572-58-2619
E-mail: itc8@nifs.ac.jp

Call for papers

The International Symposium of the Institute for Advanced Energy (ISIAE97) on Plasma Dynamics in Complex Electromagnetic Field —For Comprehension of Physics in Advanced Toroidal Plasma Confinement
December 8–11, 1997, Gokasho, Uji 611, Japan

Supported by: Monbusho (the Ministry of Education, Science, Sports and Culture)

General information: The ISIAE97 is one in a series of symposiums to be organized in 1997 by the Institute of Advanced Energy for the progress of energy research. Fusion science has been selected as the subject of ISIAE97 in order to promote our understanding of plasma behavior in toroidal confinement systems. These systems include (1) new helical systems such as helical-axis stellarators and (2) internal-current systems based on paramagnetic effects in the plasma, both recently constructed or proposed around the world.

Invited talks and contributed papers on experimental and theoretical results of currently operating toroidal devices will be given with ample presentation and discussion time. The symposium will also cover near-term plans for advanced toroidal confinement experiments. The symposium will be held in the conference room of the Institute of Advanced Energy located at the Uji campus, Kyoto University, Gokasho, Uji 611, Japan.

Topics: The symposium will be focused on the following two topics: (1) Configuration effects on plasma properties in advanced stellarators. (2) Plasma dynamics in internal current systems such as advanced tokamaks, RFP/ULQ, and compact tori.

Registration/Abstract/Publication: Those who intend to participate in the symposium are encouraged to preregister by mailing or faxing the Preregistration Form by July 7,1997. Those who present papers are requested to submit a one-page abstract (A4 size) by September 12, 1997. Contributors will be requested to prepare camera-ready manuscripts, which will be published in the Proceedings. Instructions for the manuscript will be sent to authors. The completed manuscript should be submitted to the scientific secretary during the symposium.

Deadlines:
Pre-registration: July 7, 1997.
One Page Abstract: Sept. 12, 1997.
Papers: Dec. 8, 1997

More detailed information can be obtained from the Conference Scientific Secretary, Dr. T. Mizuuchi, or the General Secretary, Ms. K. Kumabe. They may be reached at:

Institute of Advanced Energy
Kyoto University Gokasho
Uji, 611 Japan

Voice: +81-774-38-3451
Fax: +81-774-38-3535
E-mail: ISIAE97@iae.kyoto-u.ac.jp